PAPER

Check for updates

Redox nature of organics modulates multi-pollutant photocatalysis: study of Cr(VI) reduction and degradation of organics with CuNiFe LDH/C₃N₄ Heterostructures

Fariah Salam,†[a] Atarad Hussain,†[ab] Mudasar Nazir,[c] Muhammad Imran Rameel,[a] Muhammad Muzammil,[a] Faiza Rasheed, [iD][d] Faisal Nawaz, [iD][b] Syed Ansar Ali Shah,[e] Richard T. Baker, [iD][e] Muhammad Basit Yameen, [iD][f] Muhammad Zaheer, [iD][f] Muhammad Tariq Sajjad [iD][c] and Muhammad Abdullah Khan [iD]*[a]

Photocatalysis has demonstrated high redox activity in decomposing organic compounds and reducing heavy metals; however, previous studies have focused primarily on enhancing these effects or treating a few pollutants simultaneously, often overlooking the impact of the chemical nature and electronic behavior of the pollutants on their performance. This study uses a CuNiFe layered double hydroxide/ C₃N₄ composite to examine how different organic pollutants (4-nitrophenol (4-NP), 2-chlorophenol (2-CP), 4-aminophenol (4-AP), and levofloxacin (LEV)) influence Cr(VI) photoreduction and *vice versa*. Our measurements reveal that Cr(VI) reduction increased from 62.5% to 71.45% with phenolics bearing electron-withdrawing groups, indicating enhanced electron transfer. In contrast, it decreased to 58% and 41% with 4-AP and 2-CP, respectively, due to the inductive effects of their electron-donating substituents and delocalization effects, which modulate the electron density at redox-active sites and suppress overall activity. Individually, 4-NP, 2-CP, LEV, and 4-AP showed photocatalytic degradation rates of 59.15%, 57.9%, 63.01%, and 51.76%, respectively. In the presence of Cr(VI), 4-NP degradation dropped to 19.01% (competitive interaction), while 2-CP, LEV, and 4-AP removal increased to 88.37%, 68.66%, and 64.03%, respectively (synergistic effects), indicating clear redox modulation. These findings highlight the importance of understanding pollutant–photocatalyst interactions to optimize systems for multi-pollutant wastewater treatment.

Introduction

Sustainable wastewater treatment remains a major challenge, with industrial discharges of dyes, phenolic compounds, pharmaceuticals, and heavy metals severely contaminating water sources.[1] Photocatalysis has emerged as a green and effective method for wastewater treatment, using photoactive materials to harvest sunlight and generate electrons, holes, and radicals for redox reactions.[2–5] While factors like charge transfer, structural design, redox mediators, and absorption range have been widely studied, the complex interactions among multiple contaminants have only recently started to gain attention.[6–8]

Modern photocatalysis targets simultaneous pollutant removal.[9–11] Studies show that organic compounds can be oxidized while heavy metals are reduced in tandem.[12–14] For example, Ag/AgBr-decorated BiVO₄ systems achieved complete Cr(VI) reduction with 88.27% ciprofloxacin degradation,[15] AgI/BiVO₄ improved tetracycline degradation and Cr(VI) reduction through synergistic photoinduced charge carriers and redox species.[16] The dye sensitization effect also boosts photocatalytic activity, as seen with RhB and Cr(VI) photoreduction using FeVO₄/BiO₄O₅Br/BiOBr.[17] However, synergy is not guaranteed. For example, anatase-TiO₂ showed increased Cr(VI) and Cu(II) reduction rates but decreased phenol degradation.[18] Similarly, ZnFe-MMOs lowered

[a] *Renewable Energy Advancement Laboratory, Department of Environmental Sciences, Quaid-i-Azam University, 15320, Islamabad, Pakistan. E-mail: makhan@qau.edu.pk*

[b] *Department of Chemistry, University of Wah, Quaid Avenue, Wah Cantt City, 47040, Pakistan*

[c] *School of Engineering and Design, London South Bank University, 103 Borough Road, London, SE1 0AA UK*

[d] *Department of Biotechnology, Faculty of Biological Sciences, Quaid-i-Azam University, Islamabad 45320, Pakistan*

[e] *School of Chemistry, University of St. Andrews, North Haugh, St. Andrews, Fife KY16 9ST, UK*

[f] *Department of Chemistry and Chemical Engineering, Syed Babar Ali School of Science and Engineering, Lahore University of Management Sciences (LUMS), Lahore, 54792 Pakistan*

† Equal contribution.

ibuprofen removal in the presence of As(III) due to the competitive interactions of arsenic species with active redox species.[19] Similarly, the simultaneous removal of 2,4-D and Cr(VI), as well as BPA and Cr(VI), is influenced by the coexisting substances such as humic acid, Cl$^-$, HCO$_3^-$, and SO$_4^{2-}$, which interfere with the process through light attenuation, radical quenching, and competition for active sites.[20,21] Consequently, the interactions between organic and inorganic pollutants in such systems are not yet fully understood.

To address this, we investigated a CuNiFe layered double hydroxide/carbon nitride (LDH/C$_3$N$_4$) composite for simultaneous Cr(VI) reduction and degradation of selected organic compounds (4-nitrophenol, 2-chlorophenol, 4-aminophenol, and levofloxacin), chosen for their electron-donating/withdrawing characteristics. C$_3$N$_4$, known for its high physicochemical stability, cost-effectiveness, and suitable band gap (2.7 eV), can drive both oxidation and reduction but suffers from fast charge recombination.[22–24] This is mitigated through doping, surface modification, or heterojunction formation.[25–28] A layered double hydroxide (LDH), with its high surface area, layered structure, and tunable composition, promotes charge transport and limits recombination *via* metal–oxygen–metal linkages.[29,30] Their O–H bonds and structural stability further enhance photocatalytic oxidation.[31,32] Various C$_3$N$_4$-LDH heterojunctions like graphitic-C$_3$N$_4$@nickel–aluminium LDH,[33] porous g-C$_3$N$_4$/calcined-Mg–Zn–Al-LDH,[34] Ni–Co-LDH/g-C$_3$N$_4$,[35] Ni–Mn-LDH/g-C$_3$N$_4$ nanohybrid,[36] and graphitic-C$_3$N$_4$/Zn–Cr-LDH,[37] have been tested for the photocatalytic removal of pollutants from water.

Building on this, our study employed CuNiFe LDH/C$_3$N$_4$ composites to explore the photocatalytic reduction of Cr(VI) in the presence of selected organic compounds, namely 4-nitrophenol, 2-chlorophenol, 4-aminophenol, and levofloxacin. These organic compounds were selected based on their electron-donating and electron-withdrawing properties to assess how their chemical nature affects Cr(VI) reduction. Additionally, we examined key parameters, such as pH, pollutant concentration, and catalyst loading, to understand their influence on the process. Overall, this study sheds light on the interactions between organic pollutants and Cr(VI) reduction, offering valuable insights for optimizing photocatalytic systems for sustainable water treatment.

Materials and methods

Materials

All materials utilized were of analytical grade and employed without any purification. Melamine was used for the synthesis of C$_3$N$_4$. For the preparation of CuNiFe LDH, copper(II) nitrate trihydrate (Cu(NO$_3$)$_2$·3H$_2$O), nickel(II) nitrate hexahydrate (Ni(NO$_3$)$_2$·6H$_2$O), and iron(III) nitrate nonahydrate (Fe(NO$_3$)$_3$·9H$_2$O) were used. Sodium hydroxide (NaOH) and sodium carbonate (Na$_2$CO$_3$) were employed for pH adjustment.

Preparation of C$_3$N$_4$

C$_3$N$_4$ was prepared through the thermal condensation method using melamine as a precursor.[24] In a typical experiment, 5 g of melamine was heated at 550 °C in a covered ceramic crucible for 4 h at a ramp rate of 2 °C min^{-1}. The resultant yellow powder was ground in a mortar and pestle. For further purification and to minimize uncondensed moieties, C$_3$N$_4$ was reheated at a ramp rate of 5 °C min^{-1} in an open container at 500 °C for 4 h.
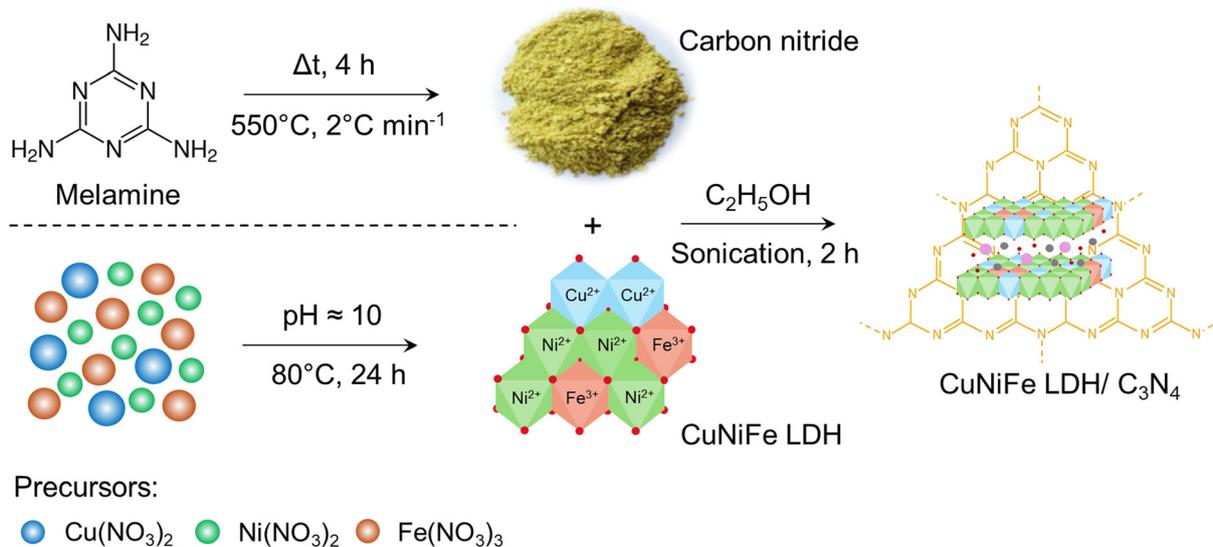
Preparation of CuNiFe LDH

CuNiFe LDH was prepared using the co-precipitation method.[38] In detail, a mixed metal salt solution in 200 mL of deionized water was prepared by adding 0.025 mol of Cu(NO$_3$)$_2$·3H$_2$O, 0.025 mol of Fe(NO$_3$)$_3$·9H$_2$O, and 0.0625 mol of Ni(NO$_3$)$_2$·6H$_2$O. An alkaline solution containing 0.8 M NaOH and 0.2 M Na$_2$CO$_3$ was then prepared. The pH of the mixed metal salt solution was adjusted to ten by adding the alkaline solution dropwise. This resulting suspension was stirred for 30 min, then aged at 80 °C for 24 h. Later, the resultant mixture was centrifuged, washed with deionized water several times, and then oven-dried for 12 h at 80 °C.

Preparation of CuNiFe LDH/C$_3$N$_4$ composite

In a typical procedure, C$_3$N$_4$ was dispersed in 20 mL of ethanol and sonicated for 30 min. Then, CuNiFe LDH was added to the solution and sonicated for 2 h. The resulting mixture was dried at 60 °C until the ethanol evaporated completely (Scheme 1). CuNiFe-LDH/C$_3$N$_4$ composites with different ratios (1:1, 1:2, 1:3, 2:1, 3:1) were systematically prepared by adjusting the amounts of C$_3$N$_4$ and CuNiFe LDH while following the same procedure.

Characterization

X-ray diffraction (XRD) data were acquired using a PANalytical X'Pert Pro diffractometer equipped with a Cu Kα radiation source (λ = 1.5418 Å), operating at 40 kV and 40 mA. Fourier-transform infrared (FTIR) analysis was performed using a Thermo Scientific Nicolet 6700 spectrometer in the range of 500–4000 cm^{-1}. The surface morphology and elemental composition of the catalysts were examined using a Zeiss Supra 55 VP FE-SEM with EDX. X-ray photoelectron spectroscopy (XPS) measurements were conducted using a Thermo Scientific K-Alpha instrument with a micro-focused monochromatic Al Kα X-ray source. Additional XPS measurements were performed in an ultrahigh vacuum chamber (~1 × 10^{-10} mbar) using a Kratos Axis Ultra DLD photoelectron spectrometer with a monochromatic Al Kα (1486.6 eV) anode, operating at 4 mA and 15 kV. High-resolution scans were recorded for C 1s, N 1s, O 1s, Cu 2p, Ni 2p, and Fe 2p. The optical properties of the synthesized samples were assessed using diffuse reflectance spectroscopy (DRS) recorded between 200 and 800 nm with a UV-2600i spectrophotometer, using BaSO$_4$ as a

This journal is © The Royal Society of Chemistry 2025

Catal. Sci. Technol., 2025, **15**, 5354–5365 | **5355**

Scheme 1 Schematic illustration of the synthesis of C_3N_4, CuNiFe LDH and CuNiFe LDH/C_3N_4 composite.

reference, to determine the band gap. Photoluminescence (PL) decay measurements were performed using an Edinburgh Instruments FLS1000 fluorimeter, with excitation at 375 nm and emission detection at 435 nm. Time-resolved photoluminescence (TRPL) spectroscopy was conducted using an Edinburgh Instruments FLS1000 spectrometer, equipped with a picosecond laser excitation source (HPL 405 nm) and a visible 980 PMT detector. Spin-trapping experiments were conducted to detect reactive oxygen species in solution. Measurements were performed using a Magnettech MS400 spectrometer, with *in situ* irradiation carried out using a 300 Xe lamp equipped with a 395 nm cut-off filter. A 10 mg amount of 5,5-dimethyl-1-pyrroline *N*-oxide (DMPO) was added to 1 mL of the reaction solution, followed by extraction of a 50 μL aliquot, which was then placed in an EPR tube for measurement.
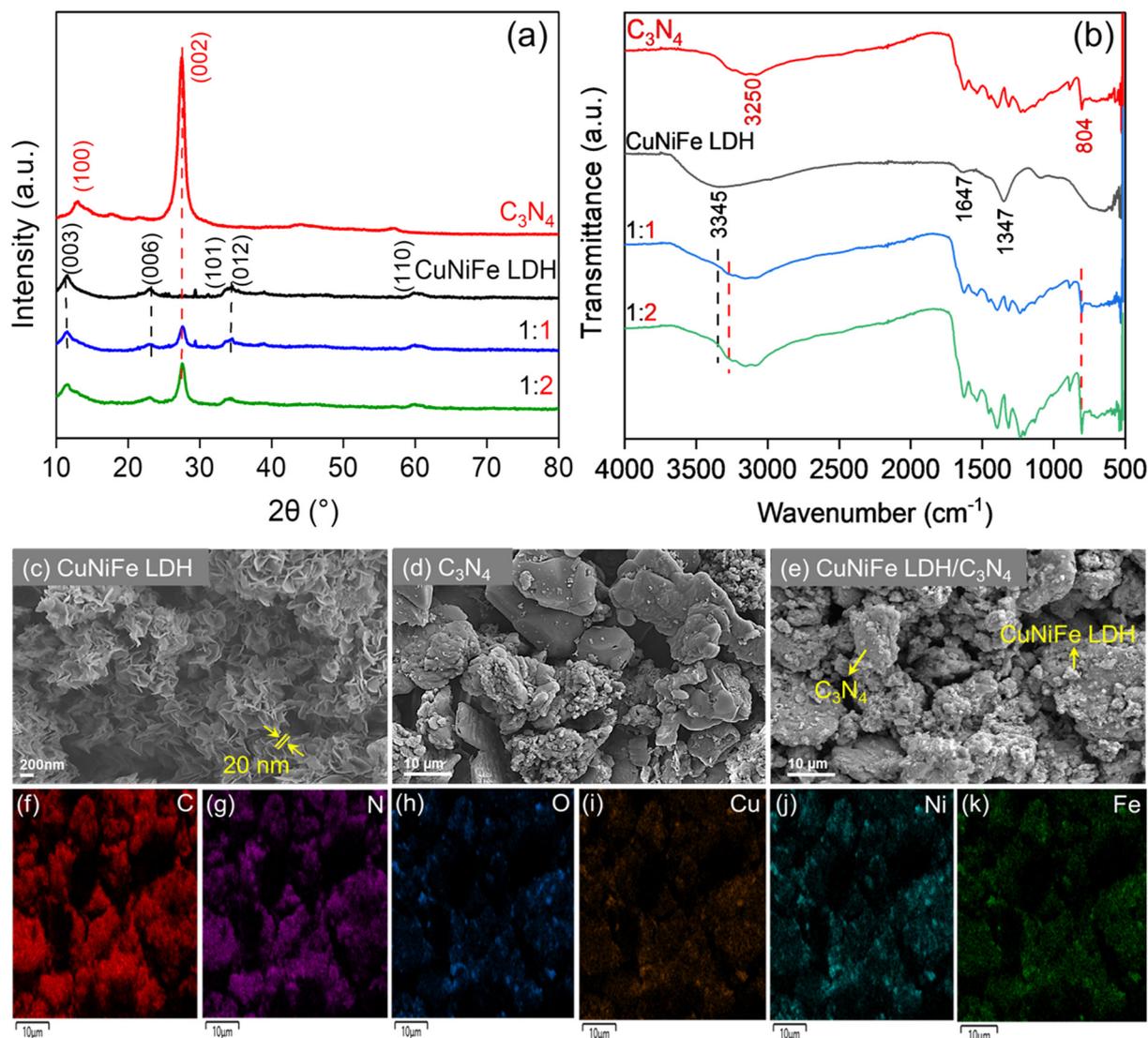
Photocatalytic activity testing

The photocatalytic performance was assessed through the degradation of various target pollutants, including phenolic compounds such as 4-nitrophenol (4-NP), 2-chlorophenol (2-CP), and 4-aminophenol (4-AP), the antibiotic levofloxacin (LEV), and the reduction of heavy metal Cr(VI). Photocatalytic experiments were performed under two distinct conditions: (i) individually (a single system), where only one pollutant was tested, and (ii) simultaneously (a binary system), where two pollutants were tested. The investigated binary systems included Cr(VI) with 4-nitrophenol (Cr(VI)–4NP), Cr(VI) with 2-chlorophenol (Cr(VI)–2CP), Cr(VI) with 4-aminophenol (Cr(VI)–4-AP), and Cr(VI) with levofloxacin (Cr(VI)–LEV). In each experiment, 0.1 g L^{-1} of the catalyst(s) was dispersed in 50 mL of a pollutant solution (10 mg L^{-1}), and the same concentrations were maintained throughout the experimental series. The reaction system was then exposed to natural sunlight, with solar illumination ranging between 90 000 and 120 000 lux (Fig. S1a). Before exposure to sunlight, the

suspension was stirred in the dark for 30 min to achieve adsorption–desorption equilibrium. At specified time intervals, 2 mL of the suspension was sampled and subsequently centrifuged (4000 rpm/5 min), and the concentration of pollutants was then determined using a UV-vis spectrophotometer. In a suspension containing Cr(VI) and organic pollutants, the maximum absorption wavelengths for 4-NP, 2-CP, 4-AP, and LEV were observed at 317 nm, 274 nm, 302 nm, and 306 nm, respectively (Fig. S2). The concentration of Cr(VI) was determined using the diphenyl-carbazide (DPC) colorimetric method, with monitoring of the purple Cr(VI)–DPC complex at 540 nm on the UV-vis spectrophotometer (Fig. S1b and S2).

Results and discussion

Structural properties of materials

Fig. 1(a) presents the XRD patterns of CuNiFe LDH, C_3N_4, and the CuNiFe LDH/C_3N_4 composite. Pristine C_3N_4 exhibits its characteristic diffraction peaks at 27.45° and 13.0°, corresponding to the (002) in-plane repeating units of heptazine and (002) interlayer stacking, respectively.[39] For CuNiFe LDH, distinct reflections appear at 11.37°, 22.80°, 34.57°, and 59.82°, which can be attributed to the (003), (006), (012), and (110) crystal planes, confirming its hydrotalcite-like layered double hydroxide structure.[40] In the CuNiFe LDH/C_3N_4 composite, peak intensities were reduced and broadened, indicating the formation of an integrated structure and interfacial interactions between constituent materials.[41] Notably, a slight shift to higher angles is observed in the (003) and (006) planes of CuNiFe LDH from 11.37° and 22.80° to 11.44° and 23.02°, respectively. A similar result is also seen in the (002) plane of C_3N_4 from 27.45° to 27.60°.[36] These subtle shifts suggest a reduction in interlayer spacing, successful integration of the materials, and the formation of a robust heterostructure (Table S1).

5356 | *Catal. Sci. Technol.*, 2025, **15**, 5354–5365

This journal is © The Royal Society of Chemistry 2025

Fig. 1 (a) XRD patterns and (b) FTIR spectra of CuNiFe-LDH, C_3N_4, and their composite (CuNiFe-LDH/C_3N_4). SEM images of (c) CuNiFe-LDH, (d) C_3N_4, and (e) CuNiFe-LDH/C_3N_4 (1 : 2). (f–k) EDS analysis of CuNiFe-LDH/C_3N_4 (1 : 2).

Fig. 1(b) presents the FTIR spectra of CuNiFe LDH, C_3N_4, and their composite (CuNiFe LDH/C_3N_4). In CuNiFe LDH, the broad bands around 3300 cm^{-1} and 1647 cm^{-1} correspond to the O–H stretching and the bending vibration of interlayer water, respectively. A sharp peak at 1347 cm^{-1} indicates the asymmetric stretching vibration of carbonate ions, which act as the primary compensating anions within the LDH interlayers.[42,43] In C_3N_4, the adsorption band between 3000 and 3300 cm^{-1} is assigned to N–H stretching vibrations. For the composite, a broad band spanning 3000–3700 cm^{-1} arises from the merged O–H and N–H stretching vibrations. Other characteristic vibrations appearing between 1200 and 1700 cm^{-1} and at 804 cm^{-1} correspond to aromatic C–N heterocycles and the bending of tri-*s*-triazine units, respectively (Fig. S3).[13,34] Additionally, a series of bands below 600 cm^{-1} in CuNiFe LDH are associated with M–O and O–M–O bond vibrations.[42] These findings confirm the

successful integration of C_3N_4 and CuNiFe LDH while retaining their distinct chemical features.

Fig. 1(c–e) show the SEM images of CuNiFe LDH, C_3N_4, and the CuNiFe LDH/C_3N_4 composite. CuNiFe LDH exhibits a flower-like morphology composed of smooth layers with an average size of ~20 nm. C_3N_4 displays an agglomerated, irregularly layered structure with numerous voids. In the CuNiFe LDH/C_3N_4 (1 : 2) composite, thin CuNiFe LDH layers uniformly cover the C_3N_4, confirming the successful formation of the heterostructure. EDS elemental mapping (Fig. 1(f–k)) shows a homogenous distribution of C, N, O, Cu, Ni, and Fe, further confirming the integrated structure. Additionally, EDX analysis (Table S2 and Fig. S4) confirms the elemental composition and proportions. BET analysis reveals a surface area of 72.91 to 87.20 m^2 g^{-1} with pore diameters between 2.12 and 11.93 nm, consistent with the reported

This journal is © The Royal Society of Chemistry 2025

Catal. Sci. Technol., 2025, **15**, 5354–5365 | **5357**

values (Table S3).[42] The relatively high specific surface area offers abundant active sites for pollutant adsorption, while the mesopores facilitate efficient mass transport during photocatalysis, highlighting the effectiveness of the synthesis strategy and its potential for enhanced catalytic performance.

Optical properties

Photocatalytic activity depends largely on light absorption. The light absorption behavior of CuNiFe LDH, C_3N_4, and their composite was examined using UV-vis DRS, as shown in Fig. 2(a). The results reveal that the absorption range of the composite is broadened, and its absorption intensity is significantly higher than that of pure C_3N_4 (445 nm), due to strong interfacial contact between C_3N_4 and CuNiFe LDH. The calculated band gaps (inset Fig. 2(a)) of CuNiFe LDH, C_3N_4, and the composite are 2.33 eV, 2.79 eV, and 2.71 eV, respectively, indicating that incorporating C_3N_4 improves light absorption and could enhance photocatalytic activity.

Photoluminescence (PL) measurements were performed to study the behaviour of photogenerated charge carriers. Fig. 2(b) shows the PL spectra for C_3N_4 and the CuNiFe LDH/C_3N_4 composites. C_3N_4 exhibits the highest PL intensity at 450 nm, indicating a higher rate of charge carrier recombination (Fig. S5). In contrast, the PL intensity decreases in the composites, with the 1:2 CuNiFe LDH/C_3N_4 sample showing the lowest intensity, implying improved charge mobility and separation. This trend is further supported by the time-resolved photoluminescence (TRPL) decay profiles in Fig. 2(c), which follow a bimolecular recombination mechanism typical for heterostructured systems. The average PL lifetime for the 1:2 composite (6.0 ns) is shorter than that of pure C_3N_4 (7.2 ns) or CuNiFe LDH (6.3 ns). Additionally, the intensity-weighted average lifetime (τ_{int}) and amplitude-weighted average lifetime (τ_{amp}) were calculated to further analyze charge carrier dynamics. The τ_{int} accounts for all excited-state populations, emphasizing longer-lived states, while the τ_{amp} reflects the contribution of each lifetime component to the total fluorescence signal. For

C_3N_4, τ_{int} and τ_{amp} are 3.96 ns and 1.45 ns, respectively, whereas for the CuNiFe LDH/C_3N_4 (1:2) composite, these values decrease to 3.66 ns and 1.006 ns. This decay behaviour and shorter lifetimes confirm that the heterostructure promotes faster charge transfer and more efficient separation of photoinduced electrons and holes (Table S4).

XPS analysis

XPS measurements were conducted to examine the surface chemical states and bonding environments of CuNiFe LDH and its CuNiFe LDH/C_3N_4 (1:2) composite. The survey spectra (Fig. 3(a)) confirm the presence of C, N, O, Fe, Ni, and Cu, with distinct peaks at 286 eV, 400 eV, 531 eV, 713 eV, 855 eV, and 934 eV, respectively. The high-resolution C 1s spectrum for CuNiFe-LDH shows peaks at 284.82 eV (C–C) and 288.9 eV (O–C=O). In the composite, additional peaks at 285.01 eV (C=N) and 286.30 eV (C–N–C) appear, along with a slightly shifted O–C=O peak at 288.52 eV, indicating electronic interactions between LDH and C_3N_4 (Fig. 3(b)).[41] The N 1s spectrum (Fig. 3(c)) exhibits a dominant peak at 398.74 eV, attributed to pyridinic N, with a shoulder at 400.64 eV corresponding to pyrrolic N.[41,44] A minor peak near 408 eV, observed only in the CuNiFe LDH sample, suggests the presence of oxidized nitrogen species. The Cu 2p spectra (Fig. 3(e)) display characteristic Cu 2p$_{3/2}$ and Cu 2p$_{1/2}$ peaks at 934.33 eV and 955.01 eV, respectively, with an energy separation of 20 eV, confirming Cu in the Cu^{2+} state.[45] Deconvolution also reveals a contribution from Cu$^+$, and a satellite peak near 967 eV further supports the presence of Cu^{2+}.

Similarly, the Ni 2p spectra (Fig. 3(f)) show peaks at 855.79 eV (Ni 2p$_{3/2}$) and 873.48 eV (Ni 2p$_{1/2}$), along with shake-up satellite peaks at 860 eV and 878 eV, confirming Ni^{2+}. Deconvolution indicates the coexistence of Ni^{2+} and Ni^{3+}, with a binding energy shift in the composite, suggesting the partial reduction of Ni^{3+} to Ni^{2+}.[46] This behavior is typical in brucite-like LDH structures, where edge-sharing MO$_6$ octahedra enable charge transfer through metal–oxygen–metal bridges, altering oxidation states.[43] According to Hund's rule, Ni^{2+} readily oxidizes to Ni^{3+}, while Cu^{2+} tends to

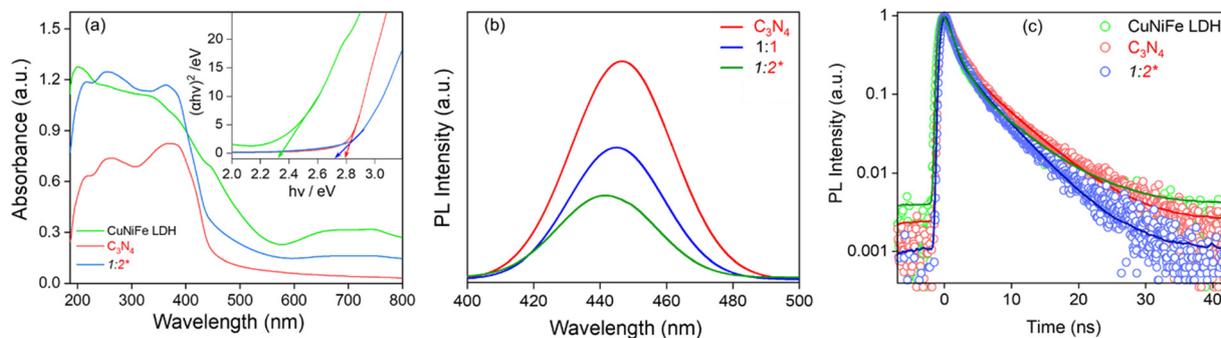**Fig. 2** (a) UV-vis DRS spectra of CuNiFe-LDH, C_3N_4, and their composite (CuNiFe-LDH/C_3N_4), with an inset showing the band gap estimation using the Tauc plot. (b) Photoluminescence (PL) spectra and (c) time-resolved PL (TRPL) decay profiles of the as-prepared samples.
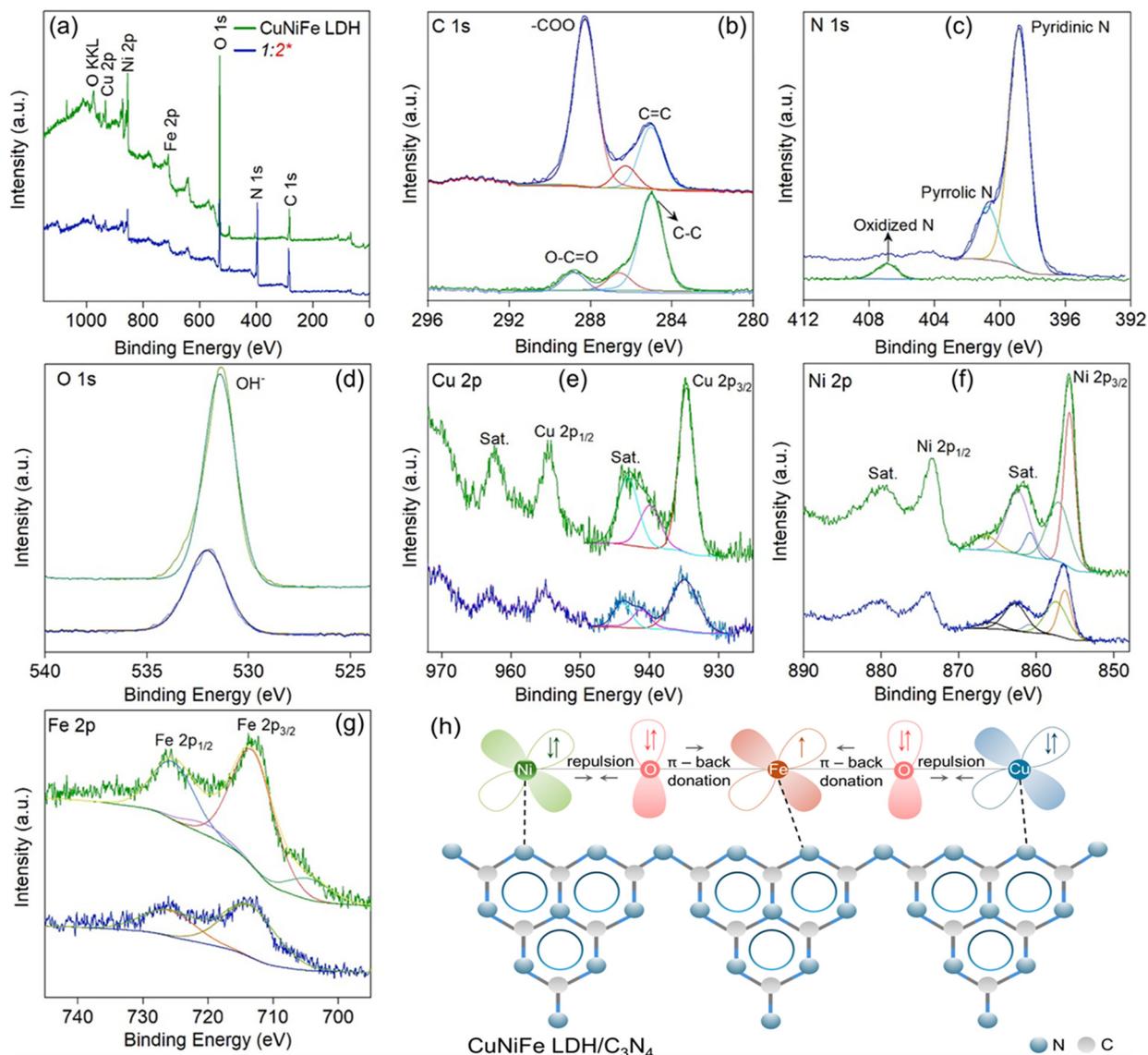
5358 | *Catal. Sci. Technol.*, 2025, **15**, 5354–5365

This journal is © The Royal Society of Chemistry 2025

Fig. 3 XPS spectra of CuNiFe-LDH and CuNiFe-LDH/C_3N_4 (1:2) composite: (a) survey spectrum, (b) C 1s, (c) N 1s, (d) O 1s, (e) Cu 2p, (f) Ni 2p, (g) Fe 2p, and (h) schematic illustration of the electronic interaction in Ni, Cu, Fe and O in CuNiFe LDH as well as with C_3N_4.

accept an electron, forming the more stable Cu$^+$.[47] These observed shifts indicate effective electron transfer between Ni and Cu within the composite. Furthermore, as shown in Fig. 3(g), the Fe 2p spectra display main peaks at 712.89 eV (Fe 2p$_{3/2}$) and 725.98 eV (Fe 2p$_{1/2}$), confirming Fe^{3+} as the dominant oxidation state.[48] The O 1s spectra show a primary peak at 531.38 eV in the pristine sample, which shifts to 532.08 eV in the composite. This shift corresponds to lattice oxygen as well as surface oxygen species, such as hydroxyl groups and adsorbed oxygen (Fig. 3(d)).[49] Overall, the slight binding energy shifts across all elemental spectra indicate structural modifications in the composite. Additionally, variations in peak intensities for C, N, Cu, Ni, Fe, and O (Table S5) suggest altered interactions and modified charge transfer dynamics that could influence catalytic performance.

A schematic of the electronic interactions among Ni, Cu, and Fe ions within the CuNiFe LDH and their interaction with C_3N_4 is illustrated in Fig. 3(h). Due to its d^8 valence electronic state configuration, Ni^{2+} has a lower affinity for O^{2-} ions and forms Ni–O bonds.[50] Fe^{3+}, with its d^5 configuration, enables π-back donation and forms an Ni–O–Fe bridge through electron transfer from Ni to Fe. Additionally, Cu^{2+} facilitates electron transfer to Fe *via* bridging O atoms, establishing an Ni–O–Fe–O–Cu pathway.[51] These metal ions (Ni^{2+}, Fe^{3+}, Cu^{2+}) also interact electrostatically with the N atoms in C_3N_4. Together with the M–O bridges, this interaction allows π-back donation from the metal's d orbitals to the conjugated π-system of C_3N_4, enhancing electron mobility, stabilizing catalytically active sites, and boosting redox activity. As a result, the composite shows strong potential as an effective photocatalyst.

Photocatalytic performance evaluation

The photocatalytic performance of CuNiFe LDH, C_3N_4, and their composites (CuNiFe LDH/C_3N_4) with varying ratios (1:1, 1:2, 1:3, 2:1, and 3:1) was evaluated for Cr(VI) reduction and 4-NP degradation to identify the optimal composition for a single photocatalytic system. In the absence of any catalyst, solar irradiation alone resulted in only a 9.2% reduction in Cr(VI) and a 7.5% decrease in 4-NP concentration due to photolysis. When CuNiFe LDH was used individually, Cr(VI) reduction reached 23.73%, and 4-NP degradation reached 26.84%. Similarly, pure C_3N_4 showed Cr(VI) reduction of 21.59% and 4-NP degradation of 17.37%. In contrast, introducing the CuNiFe LDH/C_3N_4 composites markedly enhanced photocatalytic activity, with the 1:2 ratio demonstrating the best performance, achieving a 62.5% reduction in Cr(VI) and a 59.15% degradation of 4-NP (Fig. S6a–f).

To investigate the impact of different organic compounds on Cr(VI) reduction in a binary system, a series of experiments were conducted using Cr(VI) combined with 4-NP, 2-CP, 4-AP, or LEV. The concentrations of Cr(VI) and each organic pollutant were set at 10 mg L^{-1}, which is optimal for Cr(VI) reduction in the single-pollutant system (Fig. S7). Notable pH shifts were observed when organic compounds were added to the Cr(VI) solution, initially at pH 6. In the Cr(VI)–4-NP binary system (pH 4), Cr(VI) reduction increased from 62.5% to 71.45%, while 4-NP degradation dropped sharply from 59.15% to 19%. Consequently, the Cr(VI) reduction rate increased from $4.99 \times 10^{-3} \pm 4.62 \times 10^{-4}$ to $6.8 \times 10^{-3} \pm 3.67 \times 10^{-4}$, whereas the 4-NP removal rate decreased from $4.93 \times 10^{-3} \pm 2.51 \times 10^{-4}$ to $7.155 \times 10^{-4} \pm 7.99 \times 10^{-5}$ (Fig. 4(a)). This behavior can be attributed to the strong electron-withdrawing effect of the –NO_2 group on 4-NP, which competes for photogenerated electrons, influencing the availability for both Cr(VI) and 4-NP.

In contrast, when 2-CP was used instead of 4-NP, Cr(VI) reduction decreased from 62.5% to 41%, while 2-CP degradation increased significantly from 57.5% to 88.37%. The Cr(VI) reduction rate dropped to $2.99 \times 10^{-3} \pm 1.05 \times 10^{-4}$, while the 2-CP degradation rate in the binary system increased from $4.21 \times 10^{-3} \pm 1.85 \times 10^{-4}$ to $1.054 \times 10^{-2} \pm 2.01 \times 10^{-3}$ (Fig. 4(b) and Table S6). This opposite trend likely results from the dual effect of the –Cl substituent: it withdraws electrons inductively yet can donate electrons through its lone pairs, modifying electron availability during photocatalysis. To further confirm this, another phenolic group pollutant, 4-AP, bearing an electron-donating –NH_2 group, was tested, which showed similar behavior: Cr(VI) reduction dropped to 58.01% from 62.5%, while 4-AP degradation increased from 51.76% to 64.03%, confirming the observed trend (Fig. 4(c)). Interestingly, in the Cr(VI)–LEV binary system, both Cr(VI) reduction and LEV degradation were enhanced (Fig. 4(d)). Cr(VI) reduction increased from 62.5% to 77.56%, while LEV degradation increased from 63.01% to 68.66%. We attribute this synergistic effect to an
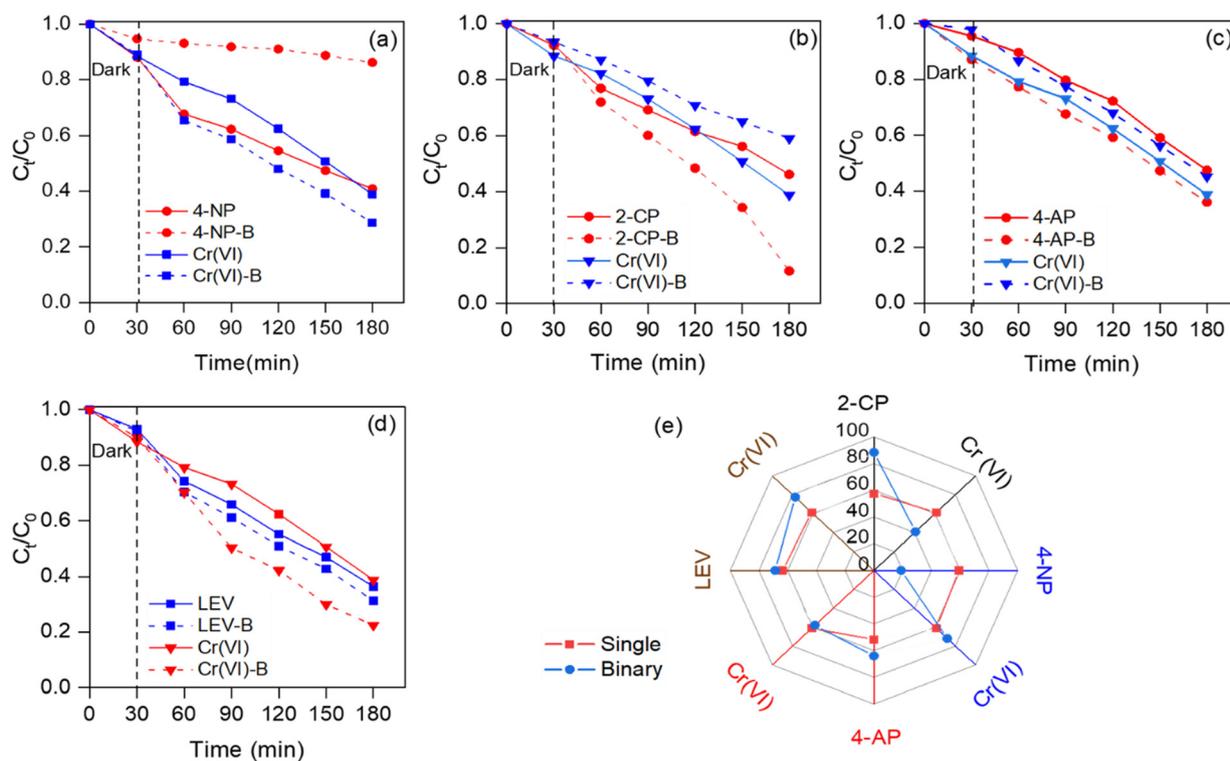

Fig. 4 Photocatalytic activity in binary systems: C_t/C_0 results for (a) Cr(VI)–4NP, (b) Cr(VI)–2CP, (c) Cr(VI)–4AP, and (d) Cr(VI)–LEV, along with (e) removal percentages for all reactions.

Table 1 Comparison of the simultaneous removal of Cr(VI) and organic compounds with the literature

System	Pollutants	Parameter	Removal efficiency	Ref.
Natural melamine/TiO$_2$	Cr(VI)–methyl orange	Catalyst: – MO: 10 mg L^{-1} Cr(VI): 30 mg L^{-1} pH: 1.5 Time: 6 h	Cr(VI) – 99.99% MO – 99.99%	53
Au–BiVO$_4$	Cr(VI)–4-chlorophenol	4-CP: 0.1 mM Cr(VI): 10 mg L^{-1} pH: – Time: 120 min	Cr(VI) – 83% 4-CP – 91%	54
N–TiO$_2$/rGO	Cr(VI)–methylene blue	Catalyst: 40 mg MB: 10 mg L^{-1} Cr(VI): 1 mg L^{-1} pH: 7 Time: –	Cr(VI) – 97.84% MB – 97.92%	55
Ag–BiVO$_4$	Cr(VI)–ciprofloxacin	Catalyst: 20 mg Cr(VI): 10 mg L^{-1} CIP: 10 mg L^{-1} Time: 60 min	CIP – 98.2% Cr(VI) – 95.63%	56
Bi$_2$S$_3$/rGO/BiVO$_4$	Cr(VI)–bisphenol-A	Catalyst: – Cr(VI): 50 ppm BPA: 10 ppm pH: 2 Time: 120 min	Cr(VI) – 100% BPA – 99.99%	10
CuNiFe LDH/C$_3$N$_4$	Cr(VI)–4-NP	Catalyst: 0.1 g L^{-1} Pollutant: 10 mg L^{-1} pH: 4 Time: 180 min	4-NP – 19% Cr(VI) – 71.45%	This work
CuNiFe LDH/C$_3$N$_4$	Cr(VI)–2-CP	Catalyst: 0.1 g L^{-1} Pollutant: 10 mg L^{-1} pH: 5 Time: 180 min	2-CP – 88.37% Cr(VI) – 40.94%	This work
CuNiFe LDH/C$_3$N$_4$	Cr(VI)–LEV	Catalyst: 0.1 g L^{-1} Pollutant: 10 mg L^{-1} pH: 6 Time: 180 min	LEV – 68.66% Cr(VI) – 77.56%	This work

electron–hole relay mechanism, where Cr(VI) effectively captures electrons, and LEV simultaneously utilizes photogenerated holes. Such mutual enhancements align with previous reports (Table 1).[52]

We also examined the photocatalytic reduction of Cr(VI) under different conditions using the 1 : 2 CuNiFe LDH/C$_3$N$_4$ composite while maintaining the Cr(VI) concentration at 10 ppm (Fig. 5(a)). Varying the solution pH from the initial pH 6 to pH 3 significantly increased the reduction efficiency from 62.5% at pH 6 to 88.4% at pH 3. This enhanced reduction at lower pH is likely due to the formation of HCrO$_4^-$ and CrO$_7^{2-}$ species, which are more readily reduced according to the reactions: HCrO$_4^-$ + 7H$^+$ + 3e$^-$ → Cr^{3+} + 4H$_2$O and Cr$_2$O$_7^{2-}$ + 14H$^+$ + 6e$^-$ → 2Cr^{3+} + 7H$_2$O. Conversely, increasing the pH to pH 9 decreased the removal of Cr(VI) to 35% (Fig. S8), likely due to the tendency of chromium to form a Cr(OH)$_3$ precipitate, which is deposited on the catalyst surface and possibly blocks active sites.[4] Additionally, the point of zero charge (pzc) for the 1 : 2 CuNiFe LDH/C$_3$N$_4$ composite was found to be 8.64 (Fig. 5(b)), indicating that the catalyst surface becomes positively charged at pH below this. This positive surface charge enhances the electrostatic attraction and adsorption of negatively charged chromium oxyanions, thereby improving the reduction efficiency.

Contribution of active species

To identify the active species involved in the redox process, radical trapping experiments were carried out by introducing specific scavengers into the photocatalytic system. Disodium ethylenediaminetetraacetate (2Na-EDTA) was used to scavenge holes (h$^+$), isopropanol (IP) for hydroxyl radicals (·OH), ascorbic acid (AA) for superoxide radicals (O$_2$·$^-$), and silver nitrate (AgNO$_3$) for electrons. As shown in Fig. 6(a), 88.4% of Cr(VI) was reduced within 180 min under sunlight irradiation at pH 3 using the 1 : 2 CuNiFe LDH/C$_3$N$_4$ composite. Notably, the addition of 2Na-EDTA and IP increased Cr(VI) reduction slightly to 91.5% and 91.7%, respectively, which can be attributed to the scavenging of h$^+$ and ·OH radicals, thereby increasing the availability of electrons for Cr(VI) reduction. In contrast, AA decreased Cr(VI) reduction to 46.2%, indicating that O$_2$·$^-$ plays a significant role in the redox process. This inhibition may result from AA promoting the preferential transfer of photogenerated electrons to molecular oxygen, thereby enhancing O$_2$·$^-$
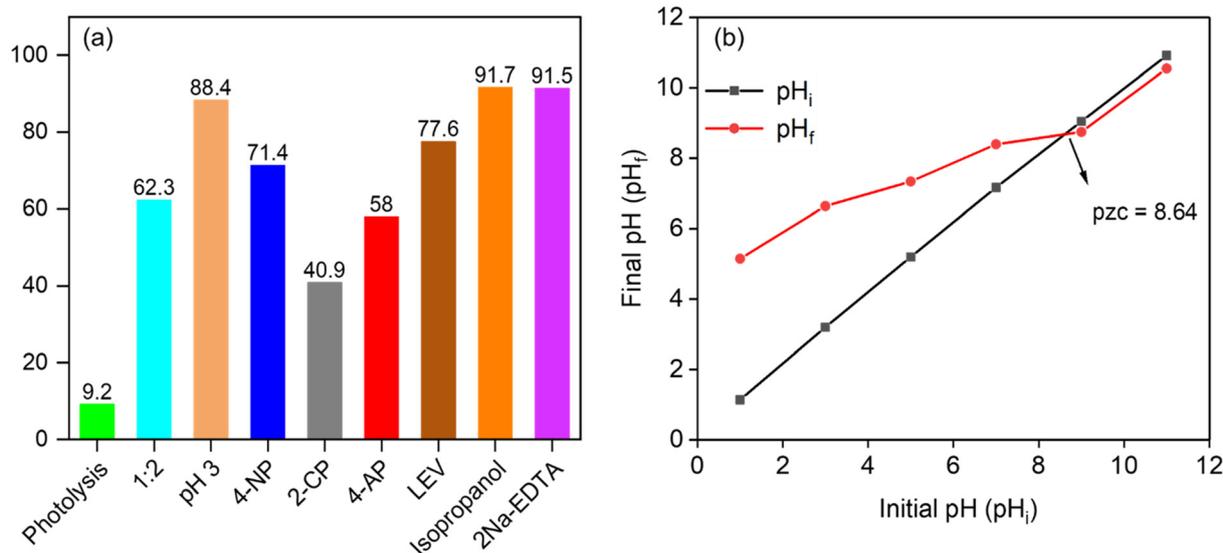
This journal is © The Royal Society of Chemistry 2025

Catal. Sci. Technol., 2025, **15**, 5354–5365 | **5361**

Fig. 5 (a) Cr(VI) photocatalytic reduction with varied experimental conditions and organic compounds, (b) point of zero charge of CuNiFe LDH/C$_3$N$_4$.
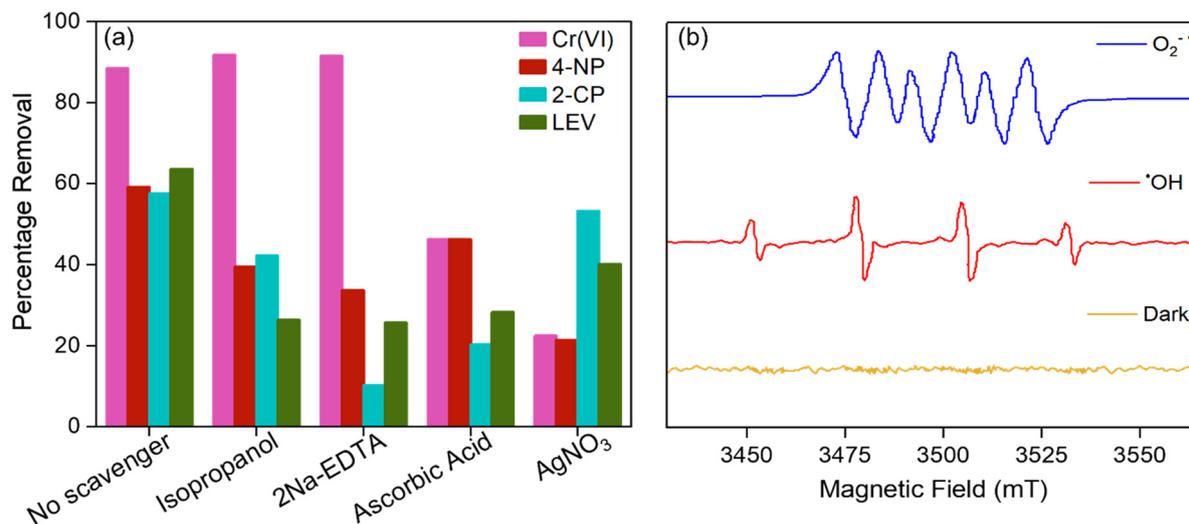

Fig. 6 (a) Effect of different scavengers on Cr(VI) reduction and the degradation of 4-NP, 2-CP, and LEV over CuNiFe-LDH/C$_3$N$_4$ (1:2). Experimental conditions: catalyst dose = 0.1 g L^{-1}, pollutant concentration = 10 mg L^{-1}, for Cr(VI) pH was adjusted to 3. (b) EPR spectra of DMPO-O$_2^{\bullet-}$ and DMPO–OH$^{\bullet}$ for CuNiFe LDH/C$_3$N$_4$ in the dark and under visible light irradiation.

formation and diverting electrons away from Cr(VI). Additionally, as a known scavenger of O$_2^{\bullet-}$, AA may further suppress Cr(VI) photoreduction by quenching these active species. Moreover, the introduction of AgNO$_3$ caused a substantial decrease in Cr(VI) reduction to 22.4% from the initial 88.4%, confirming that electrons are the primary species responsible for Cr(VI) reduction. These results demonstrate that both O$_2^{\bullet-}$ and electrons are the dominant active species for Cr(VI) reduction with the 1:2 (CuNiFe LDH/C$_3$N$_4$) composite.

For the photocatalytic degradation of 4-NP, the addition of IP and 2Na-EDTA lowered the degradation efficiency from 59.15% to 39.57% and 33.69%, respectively, indicating that

$^{\bullet}$OH and h$^+$ contribute significantly to 4-NP breakdown (Fig. 6(a)). Similarly, AgNO$_3$ reduced the degradation efficiency to 22.43%, highlighting the role of electrons. Furthermore, the addition of AA, an O$_2^{\bullet-}$ scavenger, resulted in a 17.79% efficiency loss. Overall, these findings suggest that all reactive species (electrons, O$_2^{\bullet-}$, $^{\bullet}$OH, and h$^+$) participate in 4-NP degradation, with electrons having the dominant influence. This dominant role of electrons also explains the reduced degradation of 4-NP observed in the binary system with Cr(VI), due to competition for electrons between the two pollutants (4-NP and Cr(VI)).

For 2-CP degradation, the addition of AgNO$_3$ caused only a slight decrease (4.66%) in degradation, suggesting that

5362 | *Catal. Sci. Technol.*, 2025, **15**, 5354–5365

This journal is © The Royal Society of Chemistry 2025

electrons play a minor role (Fig. 6(a)). The presence of IP results in a 15.25% decrease, implying that ·OH contributes moderately. However, the addition of AA and 2Na-EDTA significantly reduced degradation by 37.67% and 47.65%, respectively, indicating that $O_2^{·-}$ and h^+ are the primary reactive species responsible for 2-CP degradation. This explains the observed drop in Cr(VI) reduction in the Cr(VI)–2-CP binary system, as both processes rely on $O_2^{·-}$. Moreover, Cr(VI) acting as an electron trap may release more h^+, thereby boosting 2-CP degradation when both pollutants are present.

For LEV, the addition of AgNO$_3$ reduced its degradation from 63.1% to 40.1% (Fig. 6(a)). Adding IP, 2Na-EDTA, and AA further decreased LEV removal to 26.3%, 25.6%, and 28.2%, respectively, confirming that ·OH, h^+, and $O_2^{·-}$ actively contribute to its degradation. Overall, the radical trapping experiments reveal that different reactive species are involved in the photocatalytic degradation of pollutants and the reduction of Cr(VI). The competitive and synergistic interactions between these species, particularly in the presence of Cr(VI), highlight the complex dynamics that influence the efficiency of multi-pollutant photocatalytic treatments in binary systems.

Electron paramagnetic resonance (EPR) spin-trapping experiments using 5,5-dimethyl-1-pyrroline N-oxide (DMPO) were performed to detect reactive species generated by the CuNiFe LDH/C$_3$N$_4$ (1:2) composite. As shown in Fig. 6(b), no ESR signals were detected in the dark. However, under visible light irradiation, strong signals corresponding to DMPO–$O_2^{·-}$ and DMPO–·OH adducts were detected, confirming the formation of $O_2^{·-}$ and ·OH radicals. These results align with the radical scavenger experiments, further confirming the involvement of these species in the photocatalytic process and demonstrating efficient charge carrier separation within the composite.

Proposed mechanism

A simplified mechanism for the photocatalytic reduction of Cr(VI) and degradation of organic pollutants using the CuNiFe LDH/C$_3$N$_4$ composite is illustrated in Fig. 7. The corresponding band diagram (Fig. 7(a)) is constructed using the band gap value of C$_3$N$_4$ measured in this study and the band edge potentials determined in our previous work.[57] Given that Ni and Cu differ by only one atomic number, the conduction and valence band positions of CuNiFe LDH were adopted from the literature.[58] Initially, Cr(VI) and organic compounds are adsorbed onto the catalyst surface, aided by the hydroxyl groups present on CuNiFe LDH.[42] The heterostructure layered architecture offers ample active sites and surface area, promoting efficient interaction with pollutants. Upon irradiation, electrons in the valence band (VB) of C$_3$N$_4$ are excited to its conduction band (CB), leaving holes behind in the VB.[59,60] These electrons are subsequently transferred to CuNiFe LDH *via* an integrated type II heterojunction, where metal–oxo–metal linkages and MO$_6$ octahedra enable effective charge migration.[61] The transition metal ions Ni^{2+}, Fe^{3+}, and Cu^{2+} undergo redox reactions (Ni^{3+}/Ni^{2+}, Fe^{3+}/Fe^{2+}, Cu^{2+}/Cu$^+$), which sustain electron flow for Cr(VI) reduction and concurrent oxidation of organic compounds, while deterring charge recombination (Fig. 7(b)).[51] In the process, reactive oxygen species such as $O_2^{·-}$ and ·OH radicals are generated, which actively degrade organic pollutants, while Cr(VI) is reduced to Cr(III). The influence of the electronic nature of the organic compounds on Cr(VI) reduction is given in Fig. 7(c). For instance, although 4-NP does consume some photogenerated electrons, partially competing with Cr(VI), its strong electron-withdrawing substituent promotes greater overall electron flow within the system, ultimately leading to
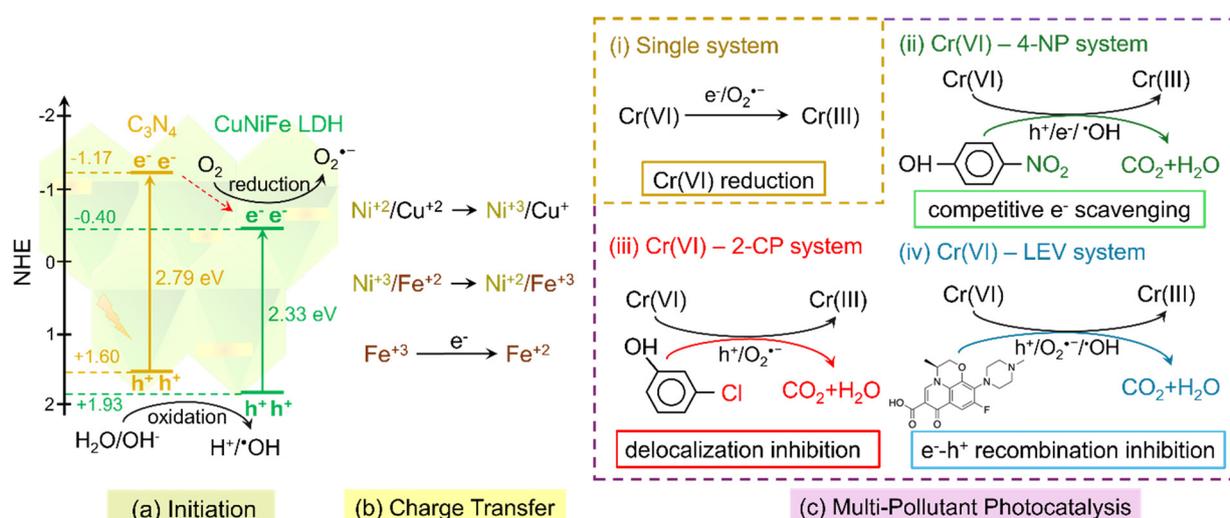
Fig. 7 Schematic of the proposed mechanism for simultaneous Cr(VI) reduction and organic pollutant degradation. (a) Photogenerated charge migration and redox initiation; (b) charge transfer within CuNiFe LDH; and (c) multi-pollutant photocatalysis. In binary systems, enhanced Cr(VI) reduction (green: Cr(VI)–4NP), decreased Cr(VI) reduction (red: Cr(VI)–2CP), and synergistic improvement in Cr(VI) reduction and LEV degradation (blue: Cr(VI)–LEV).

This journal is © The Royal Society of Chemistry 2025

Catal. Sci. Technol., 2025, **15**, 5354–5365 | **5363**

a net enhancement in Cr(VI) reduction. In contrast, 2-CP, through charge delocalization effects, reduces electron availability and thus lowers Cr(VI) reduction. LEV, however, appears to suppress charge recombination, thereby extending electron lifetimes and improving Cr(VI) reduction. Overall, the interplay between the chemical nature of coexisting organic compounds and the catalyst structure governs the efficiency of simultaneous Cr(VI) reduction and organic pollutant degradation, underlining the critical role of pollutant electronic properties and charge transfer dynamics in optimizing photocatalytic photo-redox systems.

Conclusion

In summary, CuNiFe LDH/C$_3$N$_4$ composites were successfully synthesized and evaluated for their photocatalytic performance in both single and binary (simultaneous) pollutant systems. In single-pollutant tests, the 1:2 CuNiFe LDH/C$_3$N$_4$ composite achieved removal efficiencies of 62.15% for Cr(VI), 63.01% for LEV, 59.15% for 4-NP, 57.50% for 2-CP, and 51.76% for 4-AP. In binary systems, the presence of 4-NP and LEV enhanced Cr(VI) reduction: 4-NP through its electron-withdrawing effect and LEV by suppressing electron–hole recombination. Conversely, 2-CP and 4-AP inhibited Cr(VI) reduction. This inhibition likely resulted from electron delocalization and electron-donating effects, which, respectively, reduced electron availability. Notably, organics bearing electron-withdrawing substituents (4-NP and LEV) promoted Cr(VI) reduction, whereas those having inductively electron-donating substituents or donate electrons through resonance effect (4-AP and 2-CP) suppressed it. The presence of Cr(VI) also reciprocally influenced the degradation behavior of the organics. These synergistic and competitive interactions underscore the importance of accounting for molecular-level multi-pollutant dynamics in governing the activity of photocatalytic systems. This study can be used as a guide for designing efficient photocatalytic wastewater treatment processes by regulating pollutant interactions in a similar manner.

Author contributions

Fariah Salam, Atarad Hussain: methodology, writing – original draft. Attarad Hussain, Fariah Salam, Mudasar Nazir, Imran Rameel, Muhammad Muzammil, Syed Asar Ali Shah: formal analysis, data curation, characterization. Faiza Rasheed, Faisal Nawaz, Basit Yameen, Muhammad Zaheer, Richard T. Baker, Muhammad Tariq Sajjad: characterization, writing – review & editing. Muhammad Abdullah Khan: conceptualization, supervision, writing and review.

Conflicts of interest

There are no competing interests to declare.

Data availability

All data are available in the main text or the SI materials. The raw experimental data files will be available free of cost from the corresponding author.

References

1　Z. H. Jabbar and B. H. Graimed, *J. Water Process Eng.*, 2022, **47**, 102671.

2　A. S. Mestre and A. P. Carvalho, *Molecules*, 2019, **24**, 3702.

3　M. A. Khan, A. Hussain, I. F. Teixeira, J. Y. Al-Humaidi, M. Hafeez and F. Liaqat, *Asian J. Org. Chem.*, 2023, **12**, 388.

4　U. Zahoor, M. I. Rameel, A. H. Javed, M. A. Khan, J. Y. Al-Humaidi, S. Iqbal, A. M. Aldawsari and A. Shah, *Int. J. Environ. Res.*, 2022, **16**, 1–14.

5　W. S. Koe, J. W. Lee, W. C. Chong, Y. L. Pang and L. C. Sim, *Environ. Sci. Pollut. Res.*, 2019, **27**, 2522–2565.

6　M. Ateia, M. G. Alalm, D. Awfa, M. S. Johnson and C. Yoshimura, *Sci. Total Environ.*, 2020, **698**, 134197.

7　Z. Long, Q. Li, T. Wei, G. Zhang and Z. Ren, *J. Hazard. Mater.*, 2020, **395**, 122599.

8　F. F. A. Aziz, A. A. Jalil, N. S. Hassan, A. A. Fauzi, M. S. Azami, N. W. C. Jusoh and R. Jusoh, *Environ. Res.*, 2022, **209**, 112748.

9　G. Xie, H. Wang, Y. Zhou, Y. Du, C. Liang, L. Long, K. Lai, W. X. Li, X. Tan, Q. Jin, G. Qiu, D. Zhou, H. Huo, X. Hu and X. Xu, *J. Taiwan Inst. Chem. Eng.*, 2020, **112**, 357–365.

10　Q. Liang, S. Ploychompoo, J. Chen, T. Zhou and H. Luo, *Chem. Eng. J.*, 2020, **384**, 123256.

11　M. Asjad, M. Arshad, N. A. Zafar, M. A. Khan, A. Iqbal, A. Saleem and A. Aldawsari, *Mater. Chem. Phys.*, 2021, **265**, 124416.

12　Q. Guo, G. Tang, W. Zhu, Y. Luo and X. Gao, *J. Environ. Sci.*, 2021, **101**, 351–360.

13　L. Fu, Z. Yan, Q. Zhao and H. Yang, *Adv. Mater. Interfaces*, 2018, **5**, 1801094.

14　K. L. Lim, J. C. Sin, S. M. Lam, H. Zeng, H. Lin, H. Li, L. Huang, A. R. Mohamed and J. W. Lim, *Inorg. Chem. Commun.*, 2025, **174**, 114063.

15　F. Chen, Q. Yang, Y. Wang, F. Yao, Y. Ma, X. Huang, X. Li, D. Wang, G. Zeng and H. Yu, *Chem. Eng. J.*, 2018, **348**, 157–170.

16　W. Zhao, J. Li, B. Dai, Z. Cheng, J. Xu, K. Ma, L. Zhang, N. Sheng, G. Mao, H. Wu, K. Wei and D. Y. C. Leung, *Chem. Eng. J.*, 2019, **369**, 716–725.

17　A. Chachvalvutikul, T. Luangwanta and S. Kaowphong, *J. Colloid Interface Sci.*, 2021, **603**, 738–757.

18　R. Vinu and G. Madras, *Environ. Sci. Technol.*, 2008, **42**, 913–919.

19　G. Di, Z. Zhu, H. Zhang, J. Zhu, H. Lu, W. Zhang, Y. Qiu, L. Zhu and S. Küppers, *Chem. Eng. J.*, 2017, **328**, 141–151.

5364 | *Catal. Sci. Technol.*, 2025, **15**, 5354–5365

This journal is © The Royal Society of Chemistry 2025

20 H. Zeng, J. C. Sin, S. M. Lam, H. Li, H. Lin, L. Huang, H. Huang, L. Xu, K. Dong, C. K. Goy, A. R. Mohamed and J. W. Lim, *Surf. Interfaces*, 2025, **67**, 106614.

21 J. C. Sin, S. M. Lam, H. Zeng, H. Lin, H. Li, L. Huang, S. J. Liaw, A. R. Mohamed, J. W. Lim, K. Dong and Z. Qin, *Ceram. Int.*, 2024, **50**, 5372–5383.

22 C. Hu, F. Chen, Y. Wang, N. Tian, T. Ma, Y. Zhang, H. Huang, C. Hu, F. Chen, N. Tian, Y. H. Zhang, H. W. Huang, Y. G. Wang and T. Y. Ma, *Adv. Mater.*, 2021, **33**, 2101751.

23 Y. Yu, K. Wu, W. Xu, D. Chen, J. Fang, X. Zhu, J. Sun, Y. Liang, X. Hu, R. Li and Z. Fang, *J. Hazard. Mater.*, 2021, **404**, 124171.

24 Q. Liang, Z. Li, Z. H. Huang, F. Kang and Q. H. Yang, *Adv. Funct. Mater.*, 2015, **25**, 6885–6892.

25 A. Mehtab, S. Banerjee, Y. Mao and T. Ahmad, *ACS Appl. Mater. Interfaces*, 2022, **14**, 44317–44329.

26 Z. Wang, J. Lv, J. Zhang, K. Dai and C. Liang, *Appl. Surf. Sci.*, 2018, **430**, 595–602.

27 M. I. Rameel, M. Wali, J. Y. Al-Humaidi, F. Liaqat and M. A. Khan, *Heliyon*, 2023, **9**, e20479.

28 Y. Li, Z. Xia, Q. Yang, L. Wang and Y. Xing, *J. Mater. Sci. Technol.*, 2022, **125**, 128–144.

29 M. Xu, M. Wei, M. Xu and M. Wei, *Adv. Funct. Mater.*, 2018, **28**, 1802943.

30 L. Mohapatra and K. Parida, *J. Mater. Chem. A*, 2016, **4**, 10744–10766.

31 L. Zhou, W. Zheng, Y. Ji, J. Zhang, C. Zeng, Y. Zhang, Q. Wang and X. Yang, *J. Hazard. Mater.*, 2013, **263**, 422–430.

32 R. Rashid, I. Shafiq, P. Akhter, M. J. Iqbal and M. Hussain, *Environ. Sci. Pollut. Res.*, 2021, **28**, 9050–9066.

33 G. Salehi, R. Abazari and A. R. Mahjoub, *Inorg. Chem.*, 2018, **57**, 8681–8691.

34 Y. Yu, D. Chen, W. Xu, J. Fang, J. Sun, Z. Liu, Y. Chen, Y. Liang and Z. Fang, *J. Hazard. Mater.*, 2021, **416**, 126183.

35 X. Zhang, P. Yang and S. P. Jiang, *Appl. Surf. Sci.*, 2021, **556**, 149772.

36 M. Shakeel, M. Arif, G. Yasin, B. Li and H. D. Khan, *Appl. Catal., B*, 2019, **242**, 485–498.

37 A. Khamesan, M. M. Esfahani, J. B. Ghasemi, F. Farzin, A. Parsaei-Khomami and M. Mousavi, *Adv. Powder Technol.*, 2022, **33**, 103777.

38 H. Zhang, L. C. Nengzi, Z. Wang, X. Zhang, B. Li and X. Cheng, *J. Hazard. Mater.*, 2020, **383**, 121236.

39 L. L. Liu, F. Chen, J. H. Wu, W. W. Li, J. J. Chen and H. Q. Yu, *J. Mater. Chem. A*, 2021, **9**, 10933–10944.

40 C. A. Antonyraj and S. Kannan, *Appl. Clay Sci.*, 2011, **53**, 297–304.

41 S. Nayak and K. M. Parida, *Sci. Rep.*, 2019, **9**, 1–23.

42 N. Wen, Y. Su, W. Deng, H. Zhou, M. Hu and B. Zhao, *Chem. Eng. J.*, 2022, **438**, 135570.

43 H. Wang, M. Jing, Y. Wu, W. Chen and Y. Ran, *J. Hazard. Mater.*, 2018, **353**, 53–61.

44 J. Yang, H. Wang, L. Jiang, H. Yu, Y. Zhao, H. Chen, X. Yuan, J. Liang, H. Li and Z. Wu, *J. Chem. Eng.*, 2022, **427**, 130991.

45 Y. Feng, D. Wu, Y. Deng, T. Zhang and K. Shih, *Environ. Sci. Technol.*, 2016, **50**, 3119–3127.

46 H. Hu, J. Liu, Z. Xu, L. Zhang, B. Cheng and W. Ho, *Appl. Surf. Sci.*, 2019, **478**, 981–990.

47 J. A. Nasir, M. Hafeez, M. Arshad, N. Z. Ali, I. F. Teixeira, I. McPherson, Z. ur Rehman and M. A. Khan, *ChemSusChem*, 2018, **11**, 2587–2592.

48 X. Liu, Y. Zhou, S. Sun and S. Bao, *RSC Adv.*, 2023, **13**, 31528–31540.

49 Y. Yang, Q. Zhou, L. Jiao, Q. Yin, Z. Li, Z. Zhang and Z. Hu, *Ionics*, 2022, **28**, 341–351.

50 J. Jiang, F. Sun, S. Zhou, W. Hu, H. Zhang, J. Dong, Z. Jiang, J. Zhao, J. Li, W. Yan and M. Wang, *Nat. Commun.*, 2018, **9**, 1–12.

51 D. Chanda, H. Kwon, M. M. Meshesha, J. S. Gwon, M. Ju, K. Kim and B. L. Yang, *Appl. Catal., B*, 2024, **340**, 123187.

52 J. Niu, T. He and J. Cheng, *Sep. Purif. Technol.*, 2025, **359**, 130664.

53 W. Xie, E. Pakdel, Y. Liang, D. Liu, L. Sun and X. Wang, *J. Photochem. Photobiol., A*, 2020, **389**, 112292.

54 Y. Wei, Y. Zhang, W. Geng, H. Su and M. Long, *Appl. Catal., B*, 2019, **259**, 118084.

55 M. Utami, S. Wang, M. M. Musawwa, T. E. Purbaningtias, M. Fitri, I. Yuspita, O. H. Abd-Elkader, K. K. Yadav, G. Munusamy-Ramanujam, D. Bang, S. W. Chang and B. Ravindran, *Chemosphere*, 2023, **332**, 138882.

56 M. Z. Abid, A. Ilyas, K. Rafiq, A. Rauf, M. A. Nadeem, A. Waseem and E. Hussain, *Environ. Sci.:Water Res. Technol.*, 2023, **9**, 2238–2252.

57 M. A. Khan, M. I. Rameel, F. Salam, J. Y. Al-Humaidi, G. H. Jaffari and A. M. Aldawsari, *Mater. Chem. Phys.*, 2024, **315**, 129052.

58 Z. Yang, C. Zhang, G. Zeng, X. Tan, L. Yang, J. Zhang, Z. Wu and M. Zhou, *Coord. Chem. Rev.*, 2021, **446**, 214103.

59 X. Tao, Y. Gao, S. Wang, X. Wang, Y. Liu, Y. Zhao, F. Fan, M. Dupuis, R. Li and C. Li, *Adv. Energy Mater.*, 2019, **9**, 1803951.

60 C. Liu, Y. Yu, X. Zhang and G. Wang, *J. Water Process Eng.*, 2025, **69**, 10685.

61 B. Ou, J. Wang, Y. Wu, S. Zhao and Z. Wang, *J. Chem. Eng.*, 2020, **380**, 122600.

This journal is © The Royal Society of Chemistry 2025

Catal. Sci. Technol., 2025, **15**, 5354–5365 | **5365**